Impact-responsive layer based on encapsulated solid/liquid non-Newtonian polymers

Abdelrahman Hegazy [a], Konstantinos Myronidis*[a], Michele Meo [b], Fulvio Pinto[a]
[a] Department of Mechanical Engineering, University of Bath, Claverton Down, Bath, BA2 7AY, UK
[b] Department of Aeronautics and Astronautics, University of Southampton, Southampton, SO17 1BJ,UK
*km515@bath.ac.uk

ABSTRACT

In this work, spherification was investigated as an encapsulation technique for an impact-responsive gel, with the ultimate objective of the final design being employed as protective equipment in the form of smart layers for protecting delicate goods in transit. The smart protective layers investigated utilised the controlled distribution of a polyborosiloxane based non-Newtonian polymer, namely shear stiffening gel (SSG), which can respond to an external stimulus i.e., a rapid mechanical load, by absorbing a large amount of energy, thus resulting in the protection of the aforementioned goods. At first instance, the constituents of the smart protective layers underwent mechanical characterisation, where the underlying mechanism of the SSG and its ability to absorb energy via means of a phase transition occurrence was established and quantified to be approximately five times higher compared to silicone. At a second stage, a thorough investigation of the optimal encapsulation method and geometrical arrangement was completed. The performance of the final design was assessed via static and dynamic tests which demonstrated that the layers containing SSG displayed superior performance compared to conventional ones, being able to autonomously offer protection to the substrates. In particular, the novel smart layers increased first and final compressive failure stresses by approximately 50%, whereas at the same time the maximum forces prior to failure in low velocity impact (LVI) tests were approximately 50% higher, across the investigated impact energy levels. The results of this work establish these novel smart protective layers as an ideal solution in a wide variety of applications where extremely fragile and valuable goods are in transit and impact forces need to be minimised or eliminated, such as camera lenses, electrical components, blood vials, and other medical products, overcoming the drawbacks of traditional packaging materials.

Keywords: Impact Protection, Cushioning, Shear Stiffening Gel (SSG), Spherification, Encapsulation

1. INTRODUCTION

Impact resistant materials facilitate the safety of personnel or equipment at risk of encountering dynamic loading scenarios and are used in sports equipment, protective military equipment, and as packaging solutions for fragile items [1]. For context, over 1 billion parcels with damaged products are sent to customers each year[2, 3]. Thus, developing materials with superior impact resistance is currently an area of high research interest that would benefit the packaging and parcel shipping industries [4, 5]. There are three levels of packaging for any product: primary, secondary, and tertiary. Primary packaging, also known as retail packaging, directly contacts and protects the product sold, whereas secondary and tertiary packaging group larger quantities of the product together to facilitate transportation and provide further protection [6].

Protective packaging solutions such as packing peanuts, bubble bags, and packing foam are also used as supplementary packaging materials inside boxes to provide cushioning and to protect shipped parcels from dropping, rough handling, and sudden manoeuvres [7]. On average, a parcel is dropped 17 times during its shipping journey, and encounters compression loads, cosmetic damage, shocks, and vibrations [2]. Protective packaging materials are primarily manufactured from expanded or extruded polystyrene, polyurethane foams, and paper [8]. These lightweight materials are often associated with high handling and transportation costs due to their limited reusability and bulky nature, which makes them difficult to dispose [8]. Bubble wrap, corrugated paper, and polyurethane (PU) foam are three common examples of such protective packaging materials. A quantitative comparison between the key mechanical and physical properties of all three materials is provided in Table 1 [9, 10]. The advantages and disadvantages of each material are discussed in Table 2 [11, 12]. The usefulness of each solution depends on the product, the level of impact protection required, shipping mass, and other factors. In some instances, a combination of these solutions is used to provide enhanced impact protection.

Table 1: Quantitative comparison of three packaging materials: Bubble Wrap, Corrugated Paper, and Polyurethane Foam.

	Bubble Wrap	**Corrugated Paper**	**Polyurethane Foam**
Density ($\boldsymbol{kg/m^3}$)	17	0.2 – 1 (kg / m^2)	12 – 30
Price per unit (£ / $\boldsymbol{m^2}$)	3	0.75	10
Impact Protection	Low	Low	Medium
Wrapping Compactness	Medium	High	Low
Packaging Flexibility	High	High	Medium
Reusability	Low	Low	Medium

Table 2: Qualitative comparison of three packaging materials: Bubble Wrap, Corrugated Paper, and Polyurethane Foam.

Material	**Advantages**	**Disadvantages**
Bubble Wrap	Lightweight Wrapping flexibility Versatile and available in different sizes	Not biodegradable Carbon intense manufacturing process Susceptible to permanent damage
Corrugated Paper	Cheapest solution Compact and space efficient Eco-friendly production and recyclable	Lowest impact protection Not weatherproof Contributes to global deforestation
Polyurethane Foam	Highest impact protection Good shock resistance Customisable for different products	Poor restorability (Expanding Foam) Difficult handling (Sprayed Foam) Highest density and most expensive

Bubble wrap and corrugated paper are flexible, lightweight, and cheap solutions that provide moderate impact protection. However, their longevity is constrained to a few cycles as bubble wrap is susceptible to permanent damage, and corrugated paper is not weatherproof. Both solutions are limited by their mechanical properties (impact strength particularly) which makes them mostly suitable for low impact protection applications, and therefore are not generally used to protect delicate equipment [9, 10]. When more delicate equipment need to be protected during transportation (such as optical lenses in disaster-struck scenarios) containers are generally reinforced with PU foam, which is a customisable solution that provides increased impact and shock resistance but this is coupled with an increased mass and a higher cost. PU is also used inside Peli Cases to protect delicate equipment like cameras and electronics [13]. However, despite their good properties, PU foam has poor restorability of mechanical properties, and the level of protection decreases significantly after the first impact. Also, PU foam is only reusable for the products it was tailored for, unlike bubble wrap and corrugated paper which can be interchangeably used to protect different products.

In this context, it is not surprising that over the years several researchers have focused their attention on the optimisation of these high-performance protecting layers, evaluating them in performances and failure mechanism. For instance, Seo et al. investigated the impact protection properties of rigid polyurethane (PU) foam and expanded polystyrene (EPS) foam for a small transportation package. Results showed that soft EPS foams (density: $20 - 40\ kg/m^3$) provided better impact protection compared to PU foams, with a yield stress between $100 - 200\ kPa$, and a higher specific compression strength [14]. However, EPS foams had a restorability coefficient of 0.9, which measures the ratio of the actual thickness of a specimen after a single impact to its original thickness before impact, and this limits their shock absorption characteristics beyond the first impact [15]. In another research, lightweight EPS foam-formed materials, reinforced with cellulose fibres, were trialled as an internal packaging material. These demonstrated good shock absorption, but were also limited by their durability, with a lower restorability coefficient compared to EPS foams (0.8)[8]. Hence, current EPS foam solutions provide good impact protection but are hindered by their restorability and reusability. Biodegradable materials were also researched for interior packaging applications, but trials resulted in less protective and more costly solutions, compared to synthetic plastic packaging [11].

Based on these considerations, this analysis presents an opportunity to develop a re-usable packaging material that combines the advantages of existing solutions, providing better impact protection, and good restorability compared to the solutions discussed. The developed solution could be implemented to protect delicate equipment such as camera lenses and electronic components.

In particular, this paper presents an innovative, smart, and flexible bubble wrap layer that provides increased impact resistance, with packaging flexibility and good restorability. This novel layer utilises a Shear Stiffening Gel (SSG) in its core, which is a non-linear polymer with energy absorption characteristics. During its synthesis, dynamic boron-oxygen (B-O) weak crosslinks are formed, which account for SSG's stiffening mechanism [16-18]. This mechanism is dependent on the rate of the application of an external stimulus, with low, intermediate, and high strain rates, resulting in corresponding phase transitions between viscous, rubbery, and glassy phases. At low strain rates, SSG exhibits viscous characteristics with increased flowability, as there is sufficient time for the B-O bonds to break [16]. At higher strain rates, the B-O bonds will dynamically break and reconstruct resulting in increased molecular resistance and a high stiffness at the macroscale [19], with this behaviour also resulting in the self-healing performance of SSG [20]. This phase transition, from viscous to rubbery state, is responsible for the excellent energy absorption characteristics of the SSG, with energy consumed in this process. Therefore, this favourable mechanism can be exploited for impact protection applications.

SSGs have shown promising prospects for impact protection, damping, and shock energy dissipation [17, 18]. Existing applications include introducing SSG into polyurethane foam for industrial purposes, using SSG as a filler material for a novel bulletproof helmet, and to enhance the ballistic performance of anti-impact devices without sacrificing wearing comfort **[**21**]**. Due to their polymeric nature, SSGs can be easily implemented into different structures, unlike Shear Thickening Fluids (STF) whose purely fluid nature makes very difficult to apply them in solid structural components. In a previous study we presented a SSG based multi-layered thin coating that can be applied to CFRP components to enhance their impact resistance by $50 - 70\%$, compared to uncoated samples [17]. However, this solution is not practical for packaging applications since a thick SSG layer would add too much weight and not adhere to complex geometries.

To optimise the distribution of the SSG on a larger area and allow for a higher flexibility in terms of packaging volume, this paper explores the use of the spherification technique to encapsulate SSG spheres and arrange them in a planar distribution to obtain a bubble wrap like layer. Spherification uses calcium lactate and sodium alginate solutions to make caviar pearls and bubble tea spheres in molecular gastronomy [22]. The complex alginate molecule (harvested from seaweeds) encapsulates the lactate solution to form an external membrane, and calcium ions are infused between two alginate molecules to stabilise them, as shown in **Figure 1**[23]. Spherification has not been academically demonstrated for encapsulating SSG but was explored due to simplicity and low cost that were the motivation for a successful study on encapsulating a STF suspension [24]. SSG spheres produced by spherification were wrapped into a flexible layer, using a combination of multiple polymers, and were then subjected to a series of mechanical tests to analyse their performance.

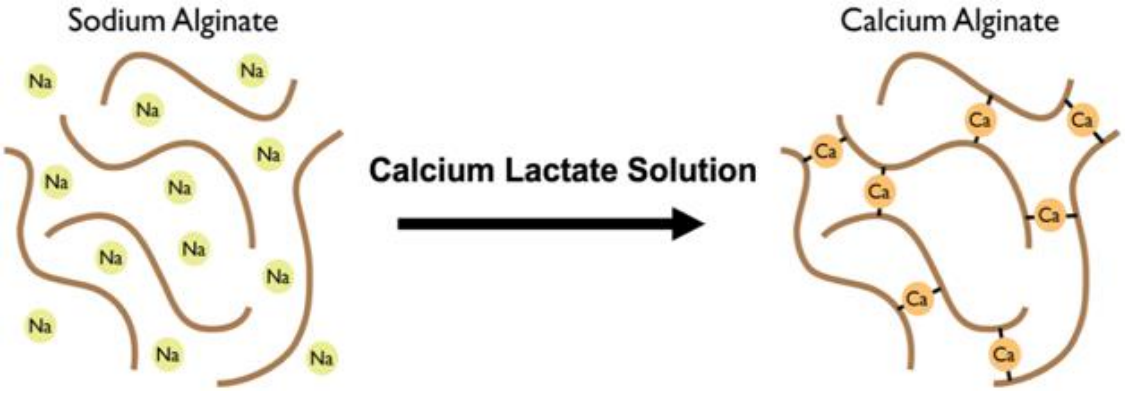

Figure 1: Spherification schematic depicting the reaction between sodium alginate and calcium lactate solutions. The product is a calcium alginate solution, with an encapsulated liquid, and calcium ions infused between two molecules to stabilise them.

2. MATERIALS AND METHODS

2.1 SSG Synthesis, Spherification, & Layer Manufacturing Process

SSGs are rate-dependent viscoelastic materials based on the synthesis of polydimethylsiloxane (PDMS) with boric acid resulting in the formation of a dynamic covalent polyborosiloxane (PBS) network, crosslinked by reversible boron-oxygen (B-O) bonds [18, 25]. A PDMS precursor with kinematic viscosity of $1K\ cSt$ and boric acid were employed in this study on a stoichiometric ratio of boron to silicon of 0.8. The materials were mechanically mixed in the presence of ethanol, to promote homogenisation of the mixture, and placed in a conventional oven at 180℃ for 72 hours. Afterwards, the solution was left to cool in room temperature and was then collected from the reacting container to be encapsulated. All reagents were purchased from Fluorchem UK and used with no further purification.

SSG spheres were manufactured by reverse spherification using 0.5% sodium alginate and 1% calcium lactate solutions [26]. Food colouring and xanthan gum (1%) were added to the calcium lactate to ensure membrane visibility and to increase the solution's viscosity respectively [26]. SSG spheres were shaped into the target diameter using 3D-printed moulds and were then placed inside the calcium lactate solution. Each sphere was covered with calcium lactate and submerged into the sodium alginate bath for encapsulation. The encapsulated SSG sphere was stirred for two minutes to allow the uniform membrane to thicken and then rinsed with distilled water. This process successfully produced spheres with a diameter between 9 and 15 mm. In order to provide a comparison for the SSG layers in terms of performance, these were compared to control samples with water spheres only (of the same mass), following an approach already established in literature where an SSG-polyurethane foam matrix was tested and compared to control samples without SSG [21, 29]. All samples were manufactured using the same process, where the type of SSG, total sphere and silicone mass, and overall sample mass were all kept constant to enable direct comparison. Manufactured samples had an average mass of $15.7g$, and the water or SSG spheres represented $2.6g$ of this value (within 10% variation).

To avoid the spheres from drying, all synthesised spheres were stored in a distilled water bath to prevent interaction with air and maintain an equal pressure on both sides of the membrane. Spheres left in air dried out since the liquid evaporated through the permeable membrane [27]. Thus, water storage provided flexibility in the manufacturing process as the spheres were produced as a batch, stored intact for some time, and wrapped into a bubble wrap layer. **Figure 2** shows the actual and cross-sectional views of control and SSG spheres manufactured by reverse spherification. The optimum ratio of an SSG sphere radius (R_{SSG}) was experimentally determined as half the total sphere radius (R_{Sphere}).

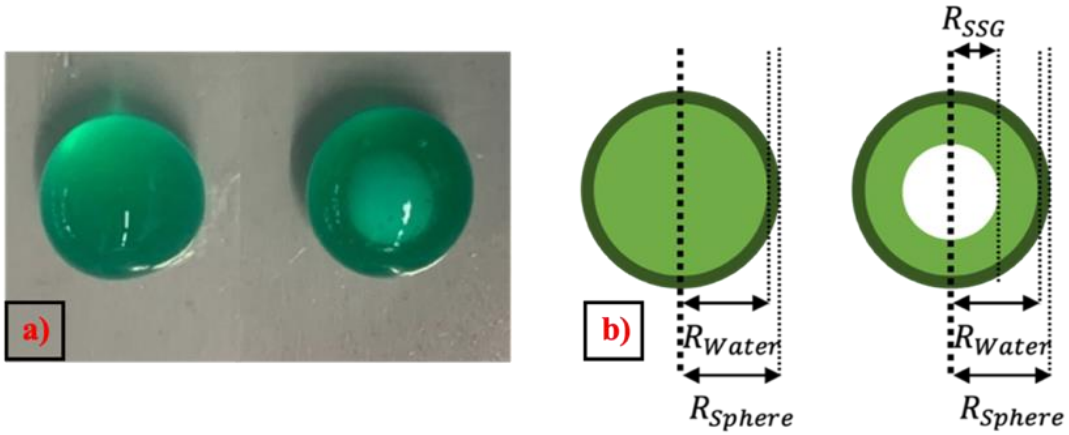

Figure 2: Comparing water and SSG spheres. a) Actual Spheres Manufactured; b) Annotated Cross-Sectional Views with white circle signifying encapsulated SSG sphere, light green annulus representing calcium lactate solution, and dark green outline representing membrane. Optimum experimental values: $R_{Sphere} = 2 * R_{SSG}$.

A wrapping process was developed and optimised to manufacture the bubble wrap layer and arrange multiple spheres in a specific geometrical arrangement. The manufactured layer was sealed with room-temperature-vulcanising (RTV) silicone, a one-component formulation. The silicone provided flexibility, supported the spheres from all directions when loaded, and did not interact with the sphere membrane. Spheres were sealed from all sides such that the top and bottom surfaces were both flush and all remaining directions were constrained. This allowed the spheres to be loaded in-plane during future tests. A polypropylene (PP) sheet was used on the bottom surface for the silicone to bond to it, and a linear low-density polyethylene (LLDPE) film was used on the top surface to facilitate manufacturing the top hemispherical profile, as shown in **Figure 3**.

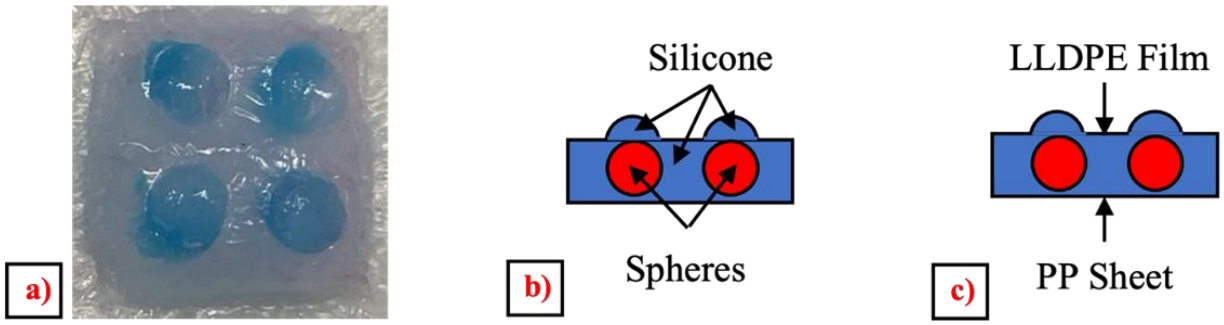

Figure 3: Optimised manufacturing process for a bubble wrap layer. a) Actual sample manufactured; b) Cross-Sectional View illustrating silicone distribution; c) Cross-Sectional View showing the bottom PP sheet and top LLDPE film.

2.2 Rheology

Rheological measurements provided insight on the relationship between the applied load and the deformation recorded at different time scales for SSGs, which have rate dependent mechanical properties [28]. The tests were performed on SSG and silicone samples using a DHR-2 rheometer from TA instruments. Oscillatory measurements over a frequency range between 0.1 and 100 Hz were conducted using a $25mm$ parallel plate configuration and the resulting Storage (G′) and Loss (G″) moduli were compared in logarithmic scales. The initial thickness of samples was measured as $2mm$ and the temperature was kept constant as 25 $°C$ during all measurements. Key comparative criteria included the storage modulus, the loss modulus, and the moduli intersection point [27].

2.3 Compression Testing

Compression tests were carried out to investigate the performance of bubble wrap layers with different sphere diameters; $9mm$, $12mm$, and $15mm$ spheres were chosen with layers of 9, 4, and 2 spheres, respectively. Three SSG and control samples were manufactured for each diameter tested, with a total sphere volume of $3600mm^3$ per layer, and an SSG volume of $450mm^3$ (for SSG samples).
A compression rate of $1mm/min$, three repeats, and a compression plate diameter of $57mm$ were defined according to the ISO 844 standard [30]. A $50kN$ load cell with an end-load condition of $10kN$ was used to record the force and crosshead displacement. The progression of a bubble wrap layer during a compression test is illustrated in **Figure 4**. Firstly, the top compression plate was moved close to the sample (**Figure 4A)**. Then the displacement at which the "spheres" were flush was recorded **(Figure 4B)**. Finally, the test continued until the $10kN$ end load condition, and the top compression plate reached the final position **(Figure 4D).**

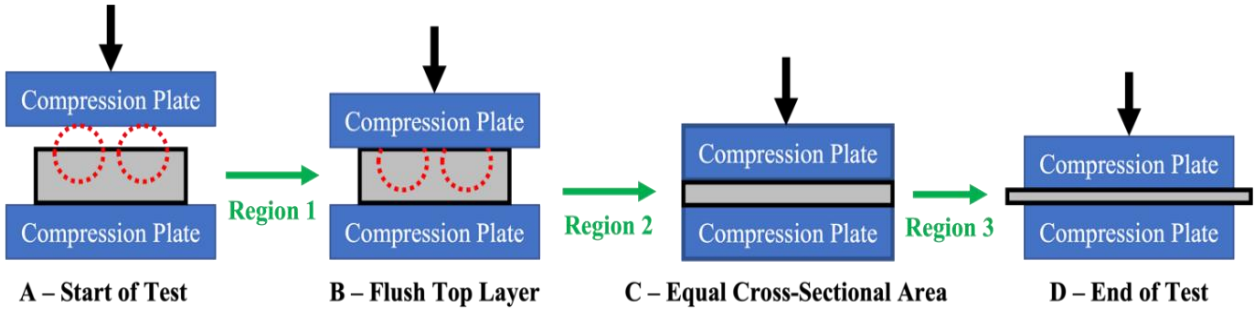

Figure 4: Progression of the bubble wrap layer during a compression test, illustrating the three key regions.

The bubble wrap layer progression during a compression test was modelled as three regions, as annotated in **Figure 4**. Initially, the hemispherical top surface was compressed until flush (region 1). The layer was then compressed until the top surface had the same compression plate diameter (region 2). Finally, the sample was compressed until failure (region 3).

The variation in cross-sectional area across the three regions was modelled to convert force readings into comparable stress values. Elastic bodies' contact theory was used to calculate the contact radius (a) between the sphere and compression plate at any displacement (δ) in region 1 [31]. Thus, the contact area in region 1 $(A_{Contact-1})$ was calculated using the number of spheres per layer (n) and the sphere radius (R_{Sphere}). Isotropic compression was assumed during region 2, and the height at which the sample and compression plate had the same cross-sectional area was determined using conservation of volume. The contact area at any point (i) during region 2 $(A_{Contact-2(i)})$ was then calculated using a linear interpolation and the contact area in region 3 $(A_{Contact-3})$ was constant and equal to the compression jig's cross-sectional area.

Hence, the contact area $(A_{Contact})$ was expressed generally for all three regions, as shown in **Equation (1)**.

$$\boldsymbol{A_{contact}} = \begin{cases} \{A_{contact-1}\} = n * \pi * a^2 \Rightarrow n * \pi * R_{sphere} * \delta \quad where\ a = \sqrt{R_{sphere} * \delta} \\ \{A_{contact-2(i)}\} = (l * w) + (i - i_0) * \left(\dfrac{\left(\dfrac{\pi * D_{compression}{}^2}{4}\right) - (l * w)}{i - i_0}\right) \\ \{A_{contact-3}\} = \dfrac{\pi * D_{compression}{}^2}{4} \end{cases} \quad (\mathbf{1})$$

Where $\boldsymbol{l}$ is the initial length of the layer (mm);

$\boldsymbol{w}$ is the initial width of the layer (mm);

$\boldsymbol{i_0}$ is the data point at which region 2 starts (flush surface);

$\boldsymbol{i}$ is the data point at which the contact area $\left(A_{Contact-2(i)}\right)$ is linearly interpolated;

$\boldsymbol{D_{Compression}}$ is the diameter of the compression plate $(57mm)$.

Therefore, the compressive stress (σ_{comp}) was calculated by dividing the force applied (N) by the respective contact area (mm^2) from **Equation (1)**. The compressive strain (ε_{comp}) was calculated by dividing the displacement (mm) by the overall sample thickness (mm), and the compression modulus (E_{comp}) in kPa was calculated as the compressive stress divided by the compressive strain. Finally, key quantitative criteria such as failure loads (N), stresses (kPa), and linear region properties were defined to compare the performance of SSG and control samples.

2.4 Low Velocity Impact Testing

LVI tests were carried out to investigate the impact properties of SSG and control samples when subjected to a dynamic event. A "square" arrangement with 9 spheres per layer ($12mm$ diameter) was chosen after analysing the compression results. **Figure 5** illustrates the wrapping process for a $12mm$ SSG sample with 9 spheres. The type of SSG, total mass of spheres and silicone, and overall sample mass were all controlled to ensure a fair comparison. Six samples were manufactured using water and SSG spheres, with an average mass of $50.6g$ and the water or SSG spheres both represented $4.6g$, which enabled direct comparison.

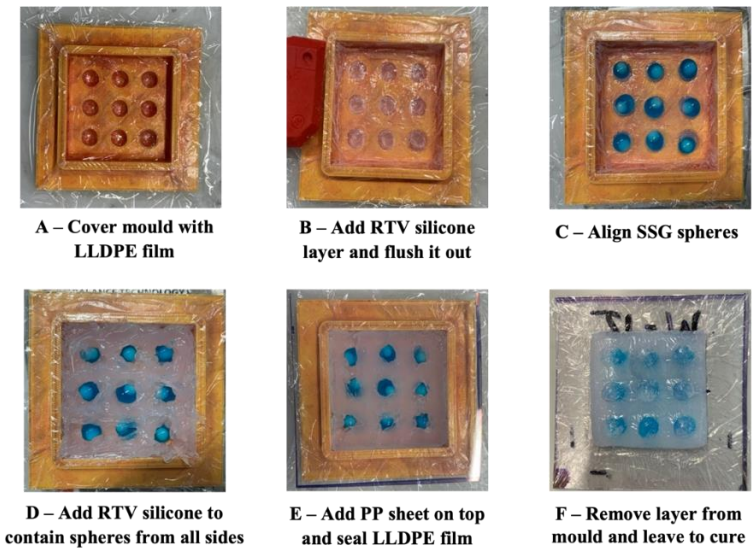

Figure 5: Bubble Wrap manufacturing process for a 12mm SSG layer with 9 spheres.

The LVI tests were performed using a drop-weight setup, where a known mass ($9.353\ kg$) equipped with a hemispherical tip (20 mm), was released on the mounted specimen, and the impact force variation with time was recorded using a loadcell [32]. The dropping height ($h_{dropping}$) corresponded to a target energy level (E_{target}) that was calculated using **Equation (2)**:

$$E_{target} = m * g * h_{dropping} \qquad \Rightarrow \qquad h_{dropping} = \frac{E_{target}}{m * g} \tag{2}$$

Where $\boldsymbol{E_{target}}$ is the target energy level (J);

$\boldsymbol{m}$ is the total impactor and shuttle mass ($9.353\ kg$);

$\boldsymbol{g}$ is the gravitational acceleration constant ($9.806\mathrm{m/s^2}$);

$\boldsymbol{h_{dropping}}$ is the dropping height (m).

Figure 6 shows the LVI test setup, with the drop masses, load cell, impactor, dropping height ruler, and clamping fixtures.

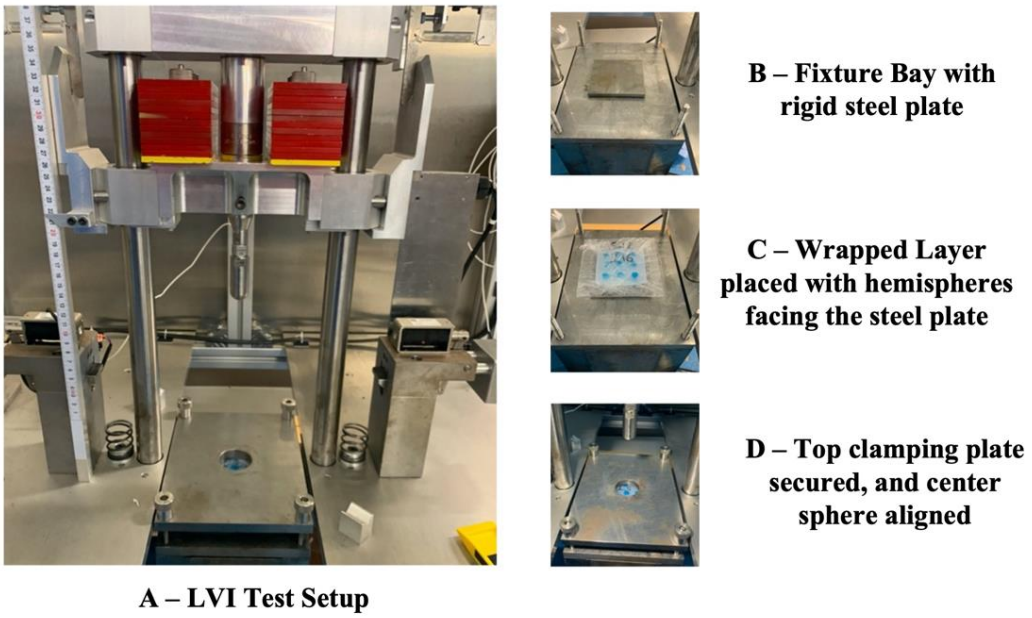

Figure 6: LVI test setup for SSG and control bubble wrap layers.

The impactor's velocity and displacement were calculated by integrating the force-time and velocity-time signals, respectively, according to ASTM D7136 standard [33], and the amount of energy absorbed during each impact was evaluated by measuring the area under the force-displacement curve [32].

All the samples were tested in reverse, at two different energy levels ($10J$ and $15J$), and three repeats were performed for each energy level and layer tested to increase reliability. The layers were placed in-reverse with the hemispheres facing a rigid steel plate, the centre sphere was aligned with the impactor tip, and then clamped with another plate, as shown in **Figure 6B – D**. Testing the layers in reverse represented the actual impact conditions for a parcel, where the bubble wrap layer is mounted internally and an external compressive load is applied, as depicted in **Figure 7A**. It also enabled contribution from other spheres during the impact, as shown in **Figure 7B**.

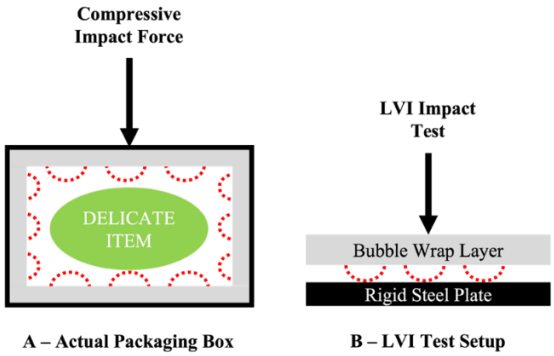

Figure 7: Cross sectional schematic of a parcel and the LVI test conditions. a) Cross Section view of actual packaging box with bubble wrap layer mounted internally to protect a delicate item; b) Replication of the compressive force applied during a LVI test, illustrating the contribution from several spheres during the impact response.

The highest impact energy level tested $(15J)$ corresponded to an impact velocity of $1.8\,m/s$ [34]. These values were calculated using **Equation (2)**, and **Equations (3)** and **(4)** below [34].

$$E_{target} = E_{Kinetic} \quad \therefore \quad \boldsymbol{m * g * h_{dropping}} = \frac{\mathbf{1}}{\mathbf{2}} * \boldsymbol{m * v_{impact}}^{\mathbf{2}} \tag{3}$$

$$\boldsymbol{v_{impact}} = \sqrt{\mathbf{2} * \boldsymbol{g} * \boldsymbol{h_{dropping}}} \tag{4}$$

Using **Equation (2)** at the Maximum Energy Level $(E_{target} = 15J) \rightarrow \boldsymbol{h_{dropping}} = \mathbf{0.1635}\boldsymbol{m}$

Using **Equation (4)** and $g = 9.806\ m/s^2 \rightarrow \boldsymbol{v_{impact}} = \mathbf{1.8}\ \boldsymbol{m/s}$

3. RESULTS

3.1 Rheology Tests

The storage (G′) and loss (G″) moduli for SSG (orange lines) and silicone (purple lines) are shown in logarithmic scales in **Figure 8,** over the measured frequencies, with continuous lines representing G′, and dashed lines G″.

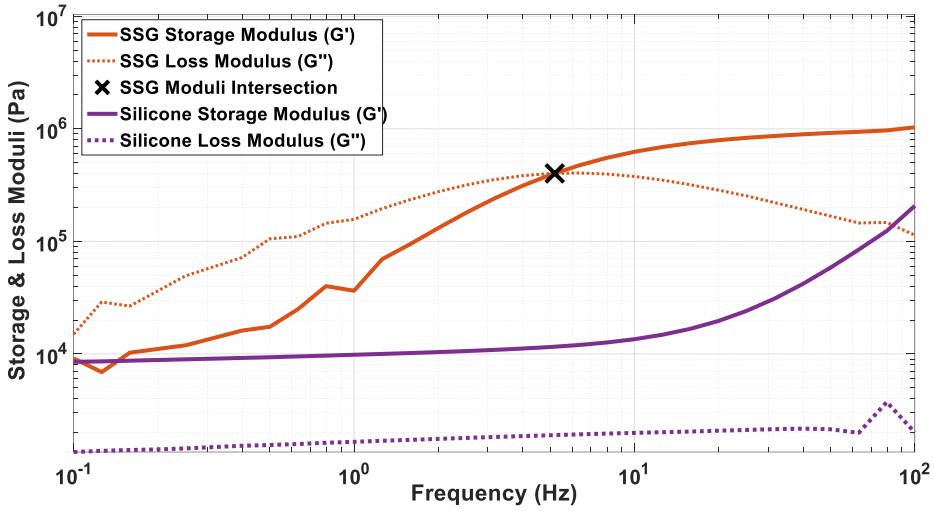

Figure 8: Variation in storage and loss moduli with frequency, for SSG (orange lines) and silicone (purple lines).

Figure 8 shows an increase in SSG's and silicone's storage moduli as the frequency increases, with both materials having a similar initial modulus, around 8.5 kPa. SSG's storage modulus increased by 991 kPa during the test to reach a maximum of 1 MPa, compared to 0.2 MPa for traditional silicone. SSG's transition point (black marker) occurs at a frequency of 5 Hz, with a corresponding modulus of 390 kPa, beyond which G′ values continued to rise and G″ started declining. On the other hand, the values of G″ for silicone increased gradually after 10 Hz and G′ values remained constant throughout the test.

3.2 Compression Tests

Figure 9 shows the stress-displacement plot for a $15mm$ bubble wrap layer with three regions of interest modelled.

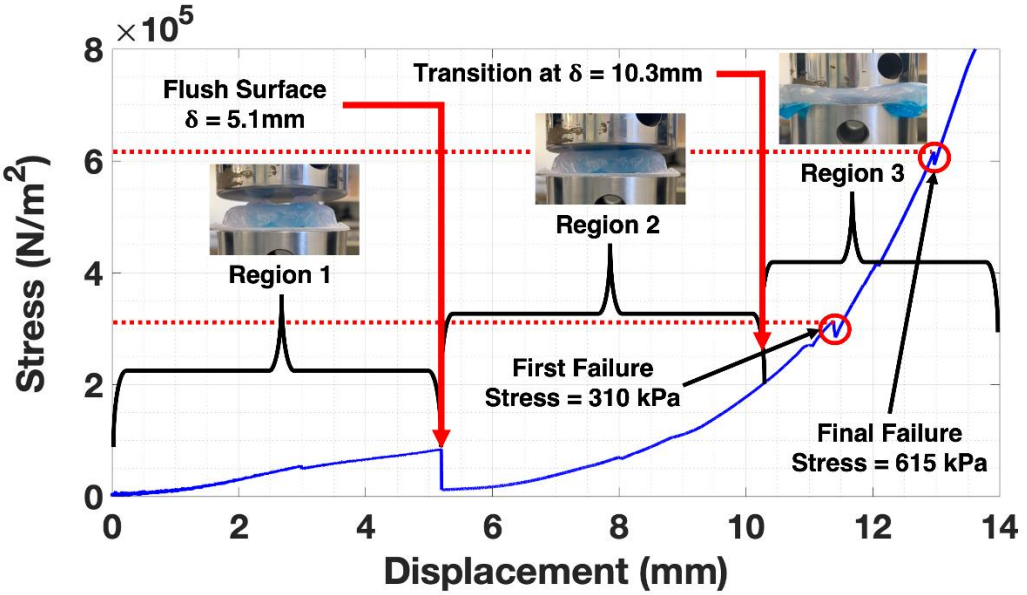

Figure 9: Stress-displacement plot for a $15mm$ bubble wrap layer, illustrating the three regions of a compression test.

A steep drop in stress occurred at the transition between regions 1 and 2, due to the cross-sectional area changing from the spheres to the full layer, as shown in **Equation (1)**. The compression modulus in region 1 was calculated using a gradient

approximation, and the maximum stress in region 1 occurred before transition to region 2. The average first and final failure stresses were calculated for all sphere diameters and samples tested using the same analytical approach, and the results are summarised in **Figure 10A** and **Figure 10B**, respectively.

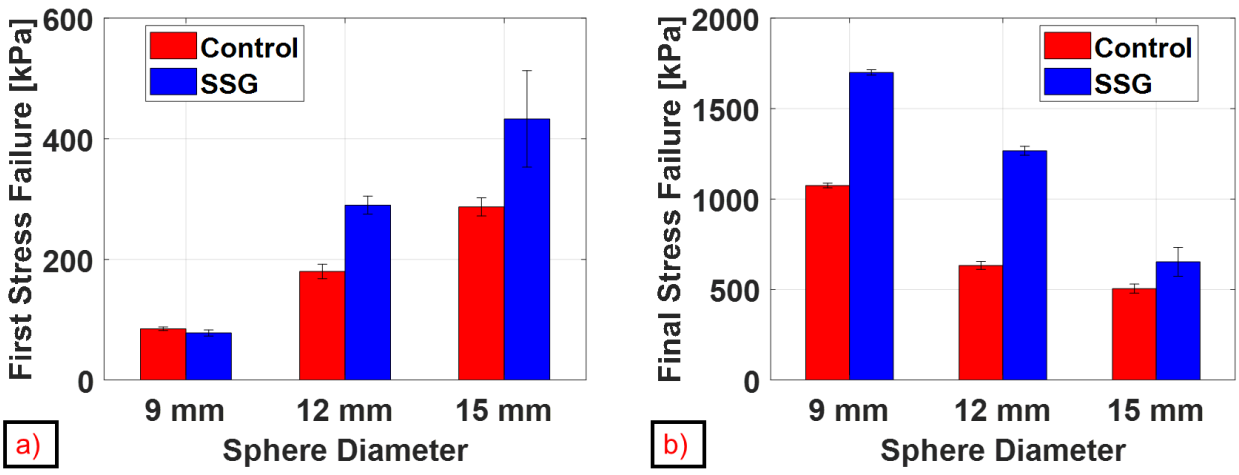

Figure 10: Comparison between the average failure stress for SSG and control samples, at all sphere diameters tested. a) First Failure Stress (kPa); b) Final Failure Stress (kPa).

As shown in **Figure 10**, SSG bubble wrap layers have a higher first and final failure stress compared to the control samples, at $12mm$ and $15mm$ sphere diameters. In addition, the first failure stress increases as the sphere diameter increases, and the final failure stress decreases as the sphere diameter increases, regardless of the layer material. Thus, $15mm$ spheres had the highest first failure stress and 9mm spheres had highest final failure stress. On average, the failure criteria were 70% higher for SSG layers, compared to the control samples. The maximum stress and compression modulus within the linear region (region 1) were also calculated, and the results are shown in **Figure 11A** and **Figure 11B**, respectively.

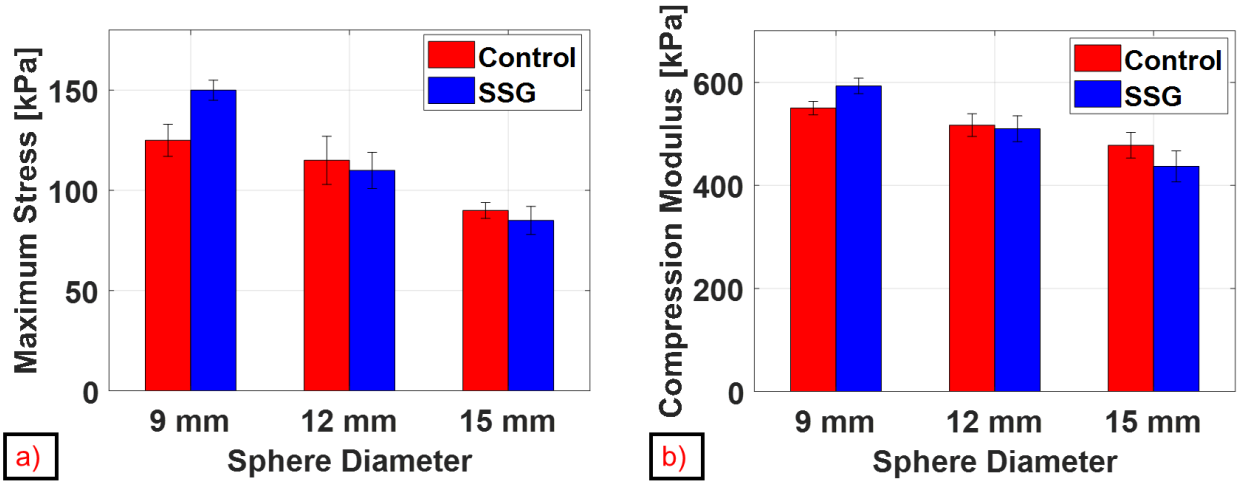

Figure 11: Comparison between the average linear region (region 1) properties for SSG and control samples, at all sphere diameters tested. a) Maximum Stress (kPa); b) Compression Modulus (kPa).

Figure 11 shows that SSG and control bubble wrap layers have a similar maximum stress and compression modulus in the linear region, at all sphere diameters tested. The difference between control and SSG layers at any sphere diameter is below 10%, with the exception of the maximum stress for $9mm$ spheres. Both plots show that the maximum stress and compression modulus slightly decrease as the sphere diameter increases, with 9mm spheres having the highest stress and compression modulus in the linear region, and $15mm$ spheres having the lowest stress and compression modulus.

3.3 LVI Tests

Figure 12 compares the control and SSG bubble wrap layers tested in LVI at $10J$ and $15J$, respectively. The force-displacement plots continued until the failure of the impacted centre sphere, which corresponded to the steep force reduction in all tests. Only one dataset is shown for clarity, but three repeats were completed for each test.

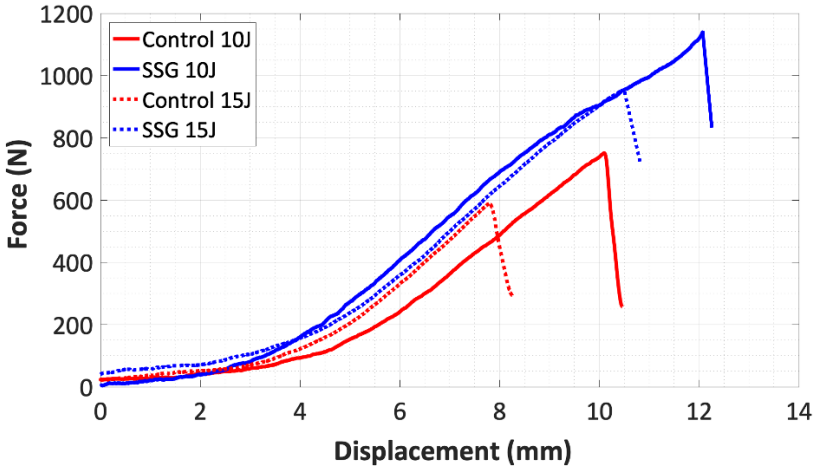

Figure 12: Force-displacement plots for SSG and control bubble wrap layers tested in LVI at $10J$ and $15J$.

As seen in **Figure 12**, SSG layers achieve a higher failure force at both energy levels tested, compared to control samples. The failure force for SSG samples is around $1150N$ (+ 53%) at $10J$ and $950N$ (+60%) at $15J$, compared to $750N$ for control samples at $10J$ and $600N$ at $15J$. Similarly, SSG samples have a larger area under the force-displacement curves, which implies that they absorbed more energy, with these values graphically illustrated in **Figure 13**.

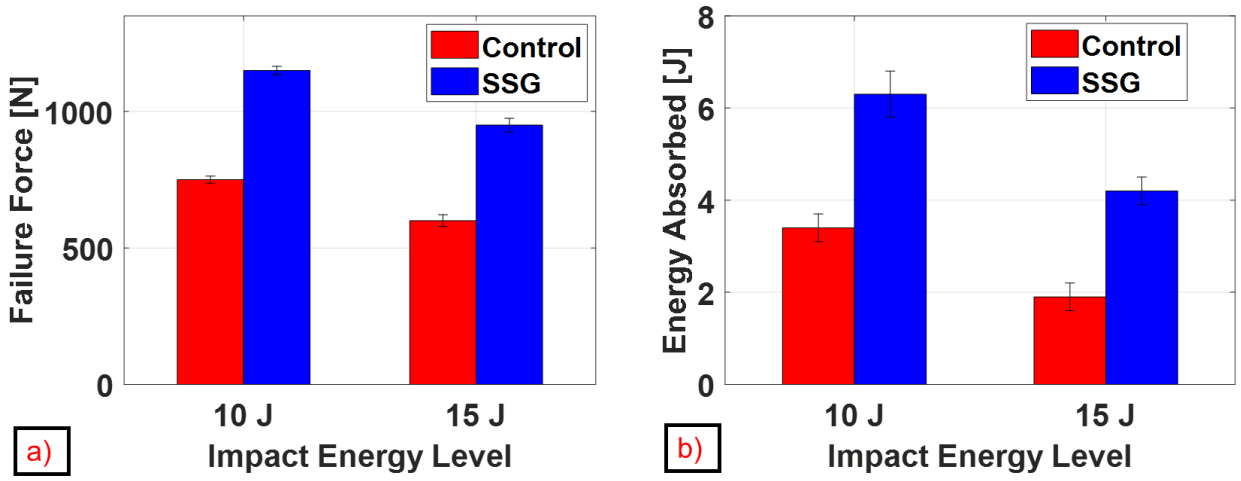

Figure 13: Average absorbed energy by control and SSG samples over impact energy levels of 10 and 15 J.

As can be appreciated in **Figure 13**, the average absorbed energy by SSG samples was $6.3J$ at an impact of $10J$, while control samples absorbed $3.4J$. Similarly, SSG samples absorbed $4.2J$ at $15J$ impact energy compared to $1.9J$ for control samples. Thus, SSG layers absorbed 80% more energy at $10J$ and 120% more energy at $15J$, compared to control samples.

4. DISCUSSION

The evolution of the curves for SSG in **Figure 8** suggest a material with clear rate-dependent properties. Initially, the values of G″ for the SSG appear to be higher than those of G′. This suggests viscous dominating properties at this regime, such that the SSG is deformable and dissipates energy as heat loss. As the oscillation frequency is increased, both moduli record greater values until their intersection point at 5 Hz, after which G′ values continued to rise and G″ started declining. At this stage, SSG transitions from viscous to rubbery state, with energy absorbed in this transition and giving rise to the SSG's stiffness. On the contrary, the moduli values did not change for the traditional RTV silicone, which suggests that the material's properties are not rate dependent. SSG's storage modulus, which relates to a material's ability to store energy, increased by $1\ MPa$, compared to $0.2\ MPa$ for silicone (between $0.1 - 100\ Hz$), which implies that SSG's variation in energy absorption is five times higher than silicone [34, 35]. This difference was more significant at intermediate frequencies ($1 - 25\ Hz$), which corresponded to the LVI tests performed. Thus, the LVI response is primarily dominated by SSG's high storage modulus, with minimal silicone contribution, despite silicone representing 80% of the total sample mass ($40g$ of $50.6g$).

Compression test results in **Figure 10A** show an increase in the first failure stress as the sphere diameter increases for both materials. This is due to the fact that samples with larger sphere diameters had fewer spheres per layer to maintain the same overall mass. Thus, the compressive load was distributed across fewer spheres, which meant that a higher force was required to initiate failure. On the other hand, the final failure stress in **Figure 10B** decreases as the sphere diameter increases since the compression force is distributed across fewer spheres after an initial failure, which meant that the final failure occurred at a lower force. On average, the failure criteria were 1.5 times higher for SSG layers, due to the SSG providing increased resistance, compared to the control samples. Generally, $12mm$ spheres were the optimum diameter since they maximised the operating range. Thereby, $12mm$ spheres provided a good balance between the first and final failure stresses, ensuring the sample can withstand initial loadings and operate for a larger window without failure.

Furthermore, **Figure 11** shows a similar maximum stress and compression modulus in the linear region for control and SSG bubble wrap layers of the same diameter. On average, both properties were within 10% for any sphere diameter, with the exception of the maximum stress for $9mm$ spheres, where SSG is higher due to measurement uncertainties. Thus, the behaviour within the linear region is primarily controlled by the sphere membrane, and the effect of SSG can be neglected. **Figure 11** also illustrates that $9mm$ layers have the highest maximum stress and compression modulus in the linear region, and both properties decrease as the sphere diameter increases, regardless of the material. This is due to $9mm$ spheres being sensitive to displacement errors and result in an underestimated contact area as per **Equation (1)**. This variation reduces for larger sphere diameters which become less sensitive to measurement errors.

The LVI plots in **Figure 12** show SSGs' superior LVI response, as the SSG layers failed at a 50% higher force than control samples at both energy levels tested. As anticipated, the full layer contributes to the impact response, and the impacted centre sphere failed in all tests. The average centre-sphere failure force for SSG layers was 1.35 times higher when tested at $10J$ compared to $15J$. This suggests that SSG samples operate better at a lower energy level, as the membrane is more likely to fail suddenly at higher energy levels. Lower energy levels also enable increased contribution from the whole layer, due to the increased response time. Likewise, the average failure force for control samples was 1.4 times higher when tested at $10J$ compared to $15J$. The average difference in failure loads between SSG and control samples was $450N$ at $10J$ and $300N$ at $15J$, reinforcing SSG's improved contribution at lower energy levels, and superior performance to water.

SSG's significantly higher storage modulus in the intermediate frequency range implies that it absorbs more energy at higher strain rates compared to silicone. Such conditions are representative of the LVI tests, and rheological results imply that silicone does not influence the impact response. As such, any noticeable difference in the impact response of SSG and control samples is primarily due to SSG's increased ability to absorb energy. Compression test results concluded that SSG bubble wrap layers had an averaged first and final failure stress that was 1.5 times higher than control samples. In general, data from LVI tests correlated to the compression test results in **Figure 10A**, where the first failure stress for $12mm$ SSG bubble wrap samples was 1.6 times higher than the control samples ($290\ kPa\ vs\ 180\ kPa$).

Finally, **Figure 14A** shows an extended bubble wrap layer inside a packaging box to transport delicate equipment, such as camera lenses, electronic components, blood vials and medical components in warzone locations. **Figure 14B** shows the flexibility of the bubble wrap layer inside a cylindrical container, illustrating the practical potential of this novel layer.

A – Small Packaging Box **B – Cylindrical Container**

Figure 14: Applications for the newly developed bubble wrap layer. a) Small Packaging Box; b) Cylindrical Container.

5. CONCLUSIONS

This paper discussed an alternative re-usable packaging solution that provides high impact protection with good packaging flexibility and restorability. The novel layer employs SSG spheres in its core, which were encapsulated by spherification, to eliminate the interaction between SSG and the external environment. A wrapping process was developed and optimised to manufacture a bubble wrap layer with multiple spheres in a specific geometrical arrangement. The optimised wrapped layer included RTV silicone to seal spheres from all sides, wrapped in a linear LLDPE film on top and bonded to a PP sheet on the bottom surface. Rheometric tests concluded that the variation in SSG's ability to absorb energy increases between $0.1 - 100\ Hz$ and is 5 times greater than silicone. This difference was more significant at intermediate frequencies ($1 - 25\ Hz$) which corresponded to the LVI tests performed. Thus, SSG's ability to absorb energy, particularly at high strain rates, implied that SSG absorbed most energy during LVI tests, as a result of its rate-dependant properties.

Samples were manufactured for compression and LVI tests using SSG spheres, and a Newtonian fluid (water) as a control for comparison. Compression tests suggested that for any sphere diameter, SSG bubble wrap samples performed better than control samples, achieving a first and final failure stresses that were 50% higher on average. Generally, increasing the sphere diameter increased the first failure stress and reduced the final failure stress due to the influence of the number of spheres per layer. The sphere membrane controlled the maximum stress and compression modulus within the linear region, and increasing the sphere diameter had a minimal effect when SSG and control samples of the same diameter were compared. LVI tests concluded that on average, SSG spheres' failure force was 50% higher than control spheres at both energy levels. Similarly, SSG samples absorbed 80% more energy at $10J$, and 120% more energy at $15J$, compared to control samples, validating the results from compression testing. Generally, SSG spheres performed better at lower energy levels due to increased contribution from the whole layer, and since the membrane fails suddenly at higher energy levels.

In conclusion, the developed layer provides increased impact resistance, with good packaging flexibility and restorability. It can be employed as a re-usable niche packaging solution to facilitate the transport of fragile equipment such as camera lenses and electronic equipment, as opposed to bubble wrap, corrugated paper, and PU foam solutions that are currently used. Finally, the practical applications of the developed bubble wrap layer were demonstrated, such as using it as an internal layer for packaging boxes or cylindrical containers to transport delicate equipment in disaster-struck scenarios.

FUNDING

The work in this publication was conducted under the project with title “Aegis, Advanced Energy-Absorption Polymer for Impact-Resistant Smart Composites” funded by the Engineering and Physical Sciences Research Council [EP/T000074/1].

REFERENCES

[1] D. Tyler, P. Venkatraman, Impact resistant materials and Design Principles for Sportswear, Proceedings of the 88th Textile Institute World Conference: Bridging Innovation, Research and Enterprise, The Textile Institute, 2012.
[2] Y. Jiang, How much a damaged pack can really cost your business, in: ECOMMERCE (Ed.) Amcor, Amcor, 2020.
[3] M. Placek, Parcel Shipping Volume Worldwide, Statista, Statista, 2022.
[4] L. Meherishi, S.A. Narayana, K. Ranjani, Integrated product and packaging decisions with secondary packaging returns and protective packaging management, European Journal of Operational Research 292(3) (2021) 930-952.
[5] M.N. PATMAYOTHIN, S. Rianmora, Alternative design for cushion packaging by applying alginate material, Thammasat University, 2021.
[6] C. Thorpe, Difference between Primary and Secondary Packaging: Domino Printing UK, Domino Printing Services, UK, 2021.
[7] Grainger, Types of Protective Packaging for Shipping, Grainger KnowHow, 2021.
[8] P. Nechita, S.M. Năstac, Overview on Foam Forming Cellulose Materials for Cushioning Packaging Applications, Polymers 14(10) (2022) 1963.
[9] Y. Gao, Research on properties and design methods of cushion packaging materials for consumer electronics, (2018).
[10] Y. Su, B. Yang, J. Liu, B. Sun, C. Cao, X. Zou, R. Lutes, Z. He, Prospects for replacement of some plastics in packaging with lignocellulose materials: A brief review, BioResources 13(2) (2018) 4550-4576.
[11] M. Dijk, Substitution of polymer interior packaging with the use of biodegradable materials, University of Twente, 2021.
[12] M. Holmes, Paper vs Traditional Bubble Wrap:All You Need to Know, UK, 2021.
[13] Brian, What Types of Foam Does Peli Use?, PELInsights, Peli UK, UK, 2022.
[14] K.S. Seo, J.C. Lee, K.S. Bang, H.S. Han, S.H. Chung, B.I. Choi, J.H. Ha, Shock absorbing evaluation of the rigid polyurethane foam and Styrofoam applied to a small transportation package, (2004).
[15] S. Nastac, C. Debeleac, P. Nechita, ASSESSMENTS ON SHOCK ABSORPTION PROPERTIES OF FOAM-FORMED LOW DENSITY CELLULOSE COMPOSITES, ACTA TECHNICA NAPOCENSIS-Series: APPLIED MATHEMATICS, MECHANICS, and ENGINEERING 60(4) (2017).
[16] K. Myronidis, M. Kopec, M. Meo, F. Pinto, A novel, bioinspired, non-Newtonian energy absorption medium for the protection of composite laminates under low velocity impact (LVI), Proc. of SPIE Vol, 2022, pp. 120410D-1.
[17] K. Myronidis, M. Thielke, M. Kopeć, M. Meo, F. Pinto, Polyborosiloxane-based, dynamic shear stiffening multilayer coating for the protection of composite laminates under Low Velocity Impact, Composites Science and Technology 222 (2022) 109395.
[18] C. Zhao, X. Gong, S. Wang, W. Jiang, S. Xuan, Shear stiffening gels for intelligent anti-impact applications, Cell Reports Physical Science 1(12) (2020) 100266.
[19] X. Li, D. Zhang, K. Xiang, G. Huang, Synthesis of polyborosiloxane and its reversible physical crosslinks, Rsc Advances 4(62) (2014) 32894-32901.
[20] M. Boccaccio, K. Myronidis, M. Thielke, M. Meo, F. Pinto, A multifunctional ultra-thin acoustic membrane with self-healing properties for adaptive low-frequency noise control, Scientific Reports 12(1) (2022) 17790.
[21] K. Myronidis, M. Meo, F. Pinto, Enhanced Anti-Impact Performance of Composite Sandwich Panels with Modified Polyurethane Foam Cores, Exploiting Phase Transition Occurence of non-Newtonian Polymer., in: A. Vasilopoulos (Ed.) ECCM20 - Composites Meet Sustainability, EPFL, Lausanne, Switzerland, 2022, pp. 63-72.
[22] K. Sivakumaran, W. Prabodhani, An overview of the applications molecular gastronomy in food industry, International Journal of Food Science and Nutrition 3(3) (2018) 35-40.

[23] S. Xu, A. Tabaković, X. Liu, E. Schlangen, Calcium alginate capsules encapsulating rejuvenator as healing system for asphalt mastic, Construction and Building Materials 169 (2018) 379-387.
[24] H. Zhang, X. Zhang, Q. Chen, X. Li, P. Wang, E.-H. Yang, F. Duan, X. Gong, Z. Zhang, J. Yang, Encapsulation of shear thickening fluid as an easy-to-apply impact-resistant material, Journal of Materials Chemistry A 5(43) (2017) 22472-22479.
[25] F.V. Drozdov, S.A. Milenin, V.V. Gorodov, N.V. Demchenko, M.I. Buzin, A.M. Muzafarov, Crosslinked polymers based on polyborosiloxanes: Synthesis and properties, Journal of Organometallic Chemistry 891 (2019) 72-77.
[26] Y.B. de Farias, C.P.Z. Noreña, Reverse encapsulation using double controlled gelification for the production of spheres with liquid light soy sauce-core, International Journal of Gastronomy and Food Science 16 (2019) 100137.
[27] B.G. Zukas, N.R. Gupta, Improved water barrier properties of calcium alginate capsules modified by silicone oil, Gels 2(2) (2016) 14.
[28] D. Zhang, N. Jiang, X. Chen, B. He, Rheology of crosslinked entangled polymers: Shear stiffening in oscillatory shear, Journal of Applied Polymer Science 137(9) (2020) 48421.
[29] S. Wang, S. Xuan, Y. Wang, C. Xu, Y. Mao, M. Liu, L. Bai, W. Jiang, X. Gong, Stretchable polyurethane sponge scaffold strengthened shear stiffening polymer and its enhanced safeguarding performance, ACS applied materials & interfaces 8(7) (2016) 4946-4954.
[30] B.S. Institution, Rigid cellular plastics - Determination of compression properties, ISO 844:2021, BSI Standards Publications, UK, 2021.
[31] Q.J. Wang, D. Zhu, Hertz Theory: Contact of Spherical Surfaces, in: Q.J. Wang, Y.-W. Chung (Eds.), Encyclopedia of Tribology, Springer US, Boston, MA, 2013, pp. 1654-1662.
[32] S. Shah, S. Karuppanan, P. Megat-Yusoff, Z. Sajid, Impact resistance and damage tolerance of fiber reinforced composites: A review, Composite Structures 217 (2019) 100-121.
[33] D. ASTM, 7136/7136M-15, Standard Test Method for Measuring the Damage Resistance of a Fiber-Reinforced Polymer Matrix Composite to a Drop-Weight Impact Event.
[34] H.A. Barnes, J.F. Hutton, K. Walters, An introduction to rheology, Elsevier1989.
[35] R. Christensen, Theory of viscoelasticity: an introduction, Elsevier2012.